



College of Engineering

Materials Science and Engineering  
434 Dougherty Engineering Building  
Knoxville, TN 37996-2200  
Phone: (865) 974-5336  
Fax: (865) 974-4115

April 27, 2009

TMS Student Awards Program  
184 Thorn Hill Road  
Warrendale, Pennsylvania 15086  
USA

Dear Whom It May Concern:

I am pleased to recommend Mr. Soo Yeol Lee, one of my full-time Ph.D. students, for taking TMS Outstanding Student Paper Contest this year.

He started his research on Neutron and X-ray Scattering Studies to investigate the Fatigue and Fracture Behaviors of Nickel-Based Superalloys since 2005. The submitted paper entitled "A Study on Fatigue-Crack-Deformation Behavior Following a Single Tensile Overload" was done by himself and is a part of his Ph.D. thesis work.

Your assistance and kind consideration of his application would be really appreciated. If you need further information about him, please feel free to contact me.

Sincerely Yours,

Dr. Peter K. Liaw  
Professor  
Ivan Racheff Chair of Excellence  
Dept. of Materials Science and Engineering  
427-B Dougherty Hall  
The University of Tennessee  
Knoxville, TN 37996-2200  
Tel: (865) 974-6356  
Fax: (865) 974-4115  
E-mail: [pliaw@utk.edu](mailto:pliaw@utk.edu)

**A Study on Fatigue-Crack-Deformation Behavior  
Following a Single Tensile Overload**

**Soo Yeol Lee**

**TMS Student Award Program:**

**Outstanding Student Paper Contest**

**Graduate Contest under the discipline of Materials Science**

**Address:**

**Soo Yeol Lee**

**Department of Materials Science and Engineering, The University of Tennessee,**

**434 Dougherty Engineering Building,  
Knoxville, TN 37996, USA**

**Tel) (865) 974 1389**

**Fax) (865) 974 4115**

**Email: [slee40@utk.edu](mailto:slee40@utk.edu)**

## Abstract

Electric-potential and neutron-diffraction experiments were performed to investigate the fatigue-crack-growth mechanisms following a single tensile overload. First, crack-opening loads were systematically measured to determine the effective-stress-intensity-factor ranges at various crack-growth stages through the retardation period using an electric-potential method. Second, residual-stress distribution in the vicinity of the fatigue-crack tip was quantitatively examined using neutron diffraction. Finally, the effects of residual stress, crack closure, and crack-tip blunting on the crack-opening load, fatigue-crack-tip-driving force, and the crack-growth behavior are investigated, and the mechanisms concerning the overload effects are suggested.

Keywords: Fatigue-crack growth; Overload; Crack closure; Electric potential; Neutron diffraction

## 1. Introduction

A fatigue-crack-propagation study is an essential part of the structural integrity-assurance-technology development based on damage-tolerance consideration. Sudden changes in the cyclic loading patterns, e.g., overload/underload, could result in transient effects, which influence the fatigue-crack-growth rate and the fatigue life. Thus, the accurate understanding for such load-interaction phenomena is of great importance for the development of the life prediction model.

One aspect that is still not completely understood is the overload effect and crack-closure mechanism in the structural materials subjected to fatigue loading. A single tensile overload introduced during constant-amplitude fatigue-crack growth results in an initial acceleration of the crack-growth rate followed by a large crack-growth-retardation period, which can increase the fatigue-life time significantly. Several possible explanations for the retardation phenomena following a tensile overload are listed below: (1) plasticity-induced crack closure [1, 2], (2) crack-tip blunting [3], (3) crack-tip strain hardening [4, 5], and (4) compressive residual stress ahead of the crack tip [6, 7]. However, the precise micromechanisms that account for these phenomena are still not fully understood, due to the difficulties to measure quantitatively strain/stress fields within the bulk sample and to observe in situ the crack-tip deformation and fracture behaviors during real-time fatigue experiments.

Recently, neutron diffraction and high-energy synchrotron X-ray diffraction as a nondestructive-evaluation technique have been employed to investigate the overload effects during fatigue-crack growth [8-11]. The deep-penetration and volume-averaging capabilities of those techniques enable the direct measurements of residual and internal strains/stresses in the bulk sample as a function of the distance from the crack tip.

In this study, neutron-diffraction and electric-potential measurements were employed to 1) study the crack-tip deformation and failure phenomena under an applied load; 2) investigate the crack-growth mechanism on cyclic deformation subjected to a single tensile overload; and 3) validate the effective-stress-intensity-factor range based on the crack-closure approach as a fatigue-crack-tip-driving force. More specifically, the effects of residual stress, crack closure, and crack-tip blunting on the crack-opening load, fatigue-crack-tip-driving force, and the crack-growth behavior will be discussed, and the mechanisms concerning the overload effects are suggested.

## 2. Experimental procedures

### 2.1 Material and Fatigue-crack-growth experiments

The fatigue-crack-growth experiments were performed on a compact-tension (CT) specimen of HASTELLOY C-2000 alloy (56%Ni-23%Cr-16%Mo, in weight percent) using a Material Test System (MTS) servohydraulic machine. This material has a single-phase face-centered-cubic (FCC) structure, yield strength of 393 MPa, ultimate tensile strength of 731 MPa, Young's modulus of 207 GPa, no preferred texture, and the average grain size of about 90  $\mu\text{m}$ . The CT specimen was prepared according to the American Society for Testing and Materials (ASTM) Standards E647-99 [12]. A constant-load-range-control ( $\Delta P$ ) mode was used for the crack-growth tests with a frequency of 10 Hz and a load ratio,  $R$ , of 0.01 ( $R = P_{\min}/P_{\max}$ ,  $P_{\min}$  and  $P_{\max}$  are the applied minimum and maximum loads, respectively). The crack length was measured by a direct-current-potential drop (DCPD) method. The stress-intensity factor,  $K$ , was obtained using the following equation [13]:

$$K = \frac{P(2 + \alpha)}{B\sqrt{W}(1 - \alpha)^{3/2}} (0.886 + 4.64\alpha - 13.32\alpha^2 + 14.72\alpha^3 - 5.6\alpha^4) \quad (1)$$

where  $P$  = applied load,  $B$  = thickness,  $\alpha = a/W$ ,  $a$  = crack length, and  $W$  = width for a CT specimen.

When the crack length reached 20 mm during a constant-amplitude fatigue-crack growth (i.e.,  $P_{\max} = 7,250$  N,  $P_{\min} = 72.5$  N), a single tensile overload (i.e.,  $P_{\text{overload}} = 10,875$  N, which is 150% of  $P_{\max}$ ) was introduced, and, then, the constant-amplitude fatigue-crack-growth test was resumed to monitor the crack-growth behavior. Figure 1 shows the crack-growth rate ( $da/dN$ ) vs. the stress-intensity-factor range,  $\Delta K$  ( $= K_{\max} - K_{\min}$ ,  $K_{\max}$  and  $K_{\min}$  are the maximum and

minimum stress-intensity factors, respectively). The crack-growth rate,  $da/dN$ , was obtained by a seven-point incremental polynomial technique [12].

## 2.2 *Electric-potential experiments*

A direct-current-potential-drop (DCPD) method was used to measure the crack length. The measured dc electric potential at any crack length was normalized and converted into the corresponding crack length using Johnson's equation [14, 15],

$$\frac{V}{V_0} = \frac{\cosh^{-1} \left[ \frac{\cosh(\pi y / W)}{\cos(\pi a / W)} \right]}{\cosh^{-1} \left[ \frac{\cosh(\pi y / W)}{\cos(\pi a_0 / W)} \right]} \quad (2)$$

where  $V_0$  and  $a_0$  are the initial crack-mouth potential and crack length, respectively;  $V$  and  $a$  are the instantaneous crack-mouth potential and crack length, respectively;  $y$  is half of the distance between the two points at which the crack-mouth potential is measured; and  $W$  is the specimen width. Using this method, the respective crack-opening load (COL) at various crack-growth stages can be determined from the curve of the normalized potential vs. applied load, as shown similarly in the previous work [16].

In this study, the changes in the electric potential during a single loading-unloading cycle were measured at eleven crack-growth stages (see Fig. 1 and Table 1) through the  $da/dN$  vs.  $\Delta K$  curve. From the plot of normalized potential vs. applied load, the bulk-averaged crack-opening loads were determined at various stages through the retardation period. Based on the measured crack-opening loads, the stress-intensity factor at the crack-tip opening,  $K_{op}$ , was calculated using Equation 1. Thus, the effective-stress-intensity-factor range,  $\Delta K_{eff}$ , was obtained using the following equation,

$$\Delta K_{\text{eff}} = K_{\text{max}} - K_{\text{op}} \quad (2)$$

where  $K_{\text{max}}$  and  $K_{\text{op}}$  denote the stress-intensity factors at the maximum load and crack opening, respectively. Finally,  $da/dN$  vs.  $\Delta K_{\text{eff}}$  was plotted to investigate the applicability of  $\Delta K_{\text{eff}}$  as a fatigue-crack-tip-driving force.

### 2.3 Residual-stress measurements using neutron diffraction

The spatially-resolved neutron residual-stress mapping was carried out on L3 spectrometer at Chalk River Laboratories, Canada. Three principal residual-strain components [i.e., transverse ( $\varepsilon_x$ ), longitudinal ( $\varepsilon_y$ ), and normal ( $\varepsilon_z$ ) strains, Fig. 2a] were measured as a function of the position from the crack tip along the crack-growth direction ( $x$ -direction, Fig. 2b). A total of 26 points were measured as a function of the distance from the crack tip. The scattering volume was positioned in the middle of the sample thickness for all strain components (Fig. 2b).

The d-spacings along the transverse, longitudinal, and normal directions were determined by the Gaussian fitting of the (311) diffraction peak and, then, the lattice strains were calculated as follows:

$$\varepsilon = (d - d_0) / d_0 \quad (3)$$

where  $d_0$  is the stress-free reference lattice spacing measured away from the crack tip. Three residual-stress components,  $\sigma_i$  ( $i = x, y,$  and  $z$ , corresponding to transverse, longitudinal, and normal directions, respectively), were calculated from three residual-strain components using the following equation:

$$\sigma_i = \frac{E}{1+\nu} \left[ \varepsilon_i + \frac{\nu}{1-2\nu} (\varepsilon_x + \varepsilon_y + \varepsilon_z) \right] \quad (4)$$

where  $E$  is the Young's modulus and  $\nu$  is the Poisson's ratio. In this study, the longitudinal residual-stress distributions near the crack tip will be presented at various crack-growth stages (i.e., 2a, 2c, and 5–7, see Table 1).

### 3. Results and discussion

#### 3.1 *Fatigue-crack-growth behavior following a single tensile overload*

Figure 1 shows the overload-induced crack-growth behavior as a function of the stress-intensity-factor range. Before the overload was applied at  $\Delta K = 35.90 \text{ MPa}\cdot\text{m}^{1/2}$ , the fatigue-crack-growth rate increased linearly with increasing  $\Delta K$ , following the Paris law. After a single tensile overload was introduced, four notable phenomena were observed: (1) an initial short acceleration of the crack-growth rate immediately after an overload, (2) the sharp decrease in the crack-growth rate down to the minimum point, (3) the gradual increase in the crack-growth rate after passing the minimum point, and (4) the recovery to the pre-overload slope in the crack-growth rate.

#### 3.2 *Crack-closure phenomena and crack-opening-load variations through the retardation period*

Figure 3a shows the electric-potential changes during a single loading-unloading cycle at the crack-growth stage 2a (a cycle just before overloading), Fig. 1. Three distinct linear regions were observed from the plot of the normalized potential vs. applied load. First, as the applied load increases up to  $0.25 P_{\max}$ , the potential increased linearly. This linear region during the loading cycle is caused by a gradual crack opening from the crack closure in the crack-wake region, i.e., the disappearance of the crack-face contact. In other words, the closed crack face from the previous unloading cycle begins to open with increasing the applied load, resulting in a significant change in the electric potential. The second linear region was observed as the applied load increases from  $0.54 P_{\max}$  to  $0.83 P_{\max}$ . In this linear region, the potential was slightly increased with the applied load. It might be due to the dominant elastic deformation at the crack

tip accompanying the elastic dimensional change of the material, after the crack tip is fully open. A transition region observed at the applied load from  $0.25 P_{\max}$  to  $0.54 P_{\max}$  might be owing to the different crack-opening levels between the surface and interior of the material. Note that the electric-potential measurement shows the bulk response of the material. The third linear region was examined as a higher load is applied from  $0.83 P_{\max}$  to  $P_{\max}$ . This linear region results from the actual crack-length increment accompanying the dominant plastic deformation at the crack tip. From such a potential measurement during a loading cycle, the bulk-averaged crack-opening load (COL) can be determined by a bilinear fitting from the first and second linear regions. Thus, the COL of  $0.34 P_{\max}$  was measured in case of the stage 2a. During unloading process, the electric potential was reduced following a reverse step.

Figure 3b shows the potential change during a single tensile loading-unloading cycle at the stage 2b (an overloading cycle) and stage 5 (a maximum retardation point). As the applied load increases up to  $P_{\text{overload}}$  ( $= 1.5 P_{\max}$ , a maximum overloading point, the stage 2b), the potential curve showed three distinct linear regions as similarly examined at the stage 2a. However, large normalized potential change of 0.04 was observed as the load was applied from  $P_{\max}$  to  $P_{\text{overload}}$ . It revealed that a tensile overload resulted in a higher increase of the actual crack advance with larger plastic deformation than that in the loading case just before overloading. During unloading after an application of tensile overload, the electric potential showed the irreversible behavior not following the loading curve. Only the potential decreased vertically down due to the elastic unloading, followed by a small transition region at lower load. As a result, it turned out that there is no crack closure in the crack wake region and only new crack face created by an overload was closed showing a small transition region.

The potential change vs. applied load at the maximum retardation (the stage 5 marked in Fig. 1) was also shown in Fig. 3b. This potential change shows quite a different behavior compared to that at the stage 2a. When the load increases up to  $0.35 P_{\max}$ , the potential did not change. It means that the closed crack face between crack-tip blunting region and actual crack-tip position does not open (i.e., crack arrest), even though the load were imposed from  $P_{\min}$  to  $0.35 P_{\max}$ . As a higher load was introduced, the electric potential began to increase linearly ( $0.35 P_{\max} \sim 0.59 P_{\max}$ ), followed by a transition region ( $0.59 P_{\max} \sim 0.68 P_{\max}$ ) and a slight increase of the potential ( $0.68 P_{\max} \sim P_{\max}$ ), corresponding to the gradual closed-crack opening, crack-tip fully opening, and the dominant elastic loading, respectively. During unloading, the crack was closed again following a reverse step of a loading curve. From the bilinear fitting, high bulk-averaged COL of  $0.63 P_{\max}$  was obtained at the maximum retardation point (stage 5).

Figure 4 shows scanning-electron microscope (SEM) micrographs at the crack tip without load before and after the overload, and at the stage 5. Before overloading (Fig. 4a), the crack was completely closed, while the crack-tip blunting was clearly observed with a few secondary cracks near the tip after the overloading (Fig. 4b), confirming that there is no crack-face contact. Fig. 4c (stage 5) showed that the crack-tip blunting still remained and the fatigue crack was closed in the crack-wake region, where further cyclic deformation was applied after the tensile overloading.

Figure 5 shows the potential measurements during a single loading-unloading cycle and COL variations at various crack-growth stages through the retardation period. At the stage 1 (constant-amplitude fatigue-crack growth before overloading), a loading and unloading potential curve showed the reversible behavior and the COL of  $0.34 P_{\max}$  was measured. At the stage 2b (an overloading cycle), the potential curve showed the irreversible behavior indicating that the

crack closure did not occur and the COL sharply dropped down. As the crack propagated to the stage 5 (a maximum retardation point) after applying a single tensile overload, the largest crack arrest portion appeared up to  $0.35 P_{\max}$ , which resulted in the highest COL of  $0.63 P_{\max}$ . When the crack grew from the stages 5 to 9, the crack arrest portion became smaller and it was completely disappeared at the stage 9, which led to a gradual decrease of the COL (COL of the stage 9 =  $0.16 P_{\max}$ ). Finally, the shape of potential curve at the stage 9 was similar to the stage 1, which supported that the crack-growth rate was already fully recovered to a pre-overload slope. As the crack grew further to the stage 11, the COL became smaller and finally zero at the stage 11. More details for COL variations are presented in Fig. 6a. As observed from the potential measurements through the  $da/dN$  vs.  $\Delta K$  curve, it should be noted that such changes in the COL are related to those in the experimentally measured crack-growth rate (Fig. 1).

### 3.3 Correlation between the crack-growth behavior and $\Delta K_{\text{eff}}$

Figure 6b shows the effective-stress-intensity-factor range ( $\Delta K_{\text{eff}}$ ) vs.  $\Delta K$  at eleven crack-growth stages marked in Fig. 1. As the  $\Delta K$  increases from the stages 1 to 2a (cycle just before overloading), the  $\Delta K_{\text{eff}}$  increased from 20.95 to 23.93  $\text{MPa}\cdot\text{m}^{1/2}$ . Immediately after a single tensile overload was introduced (the stage 2c), the  $\Delta K_{\text{eff}}$  increased instantaneously to 34.27  $\text{MPa}\cdot\text{m}^{1/2}$ , which corresponds to an instantaneous acceleration of the crack-growth rate. At the stages 3, 4, and 5, the  $\Delta K_{\text{eff}}$  sharply decreased with increasing the  $\Delta K$ . Note that the minimum  $\Delta K_{\text{eff}}$  of 13.84  $\text{MPa}\cdot\text{m}^{1/2}$  was obtained at the stage 5 (the lowest crack-growth-rate point within the retardation period). This trend was consistent with a sharp decrease in the crack-growth rate after the tensile overloading (stages 3–5 in Fig. 1). As the crack propagates further from the stages 5 (a maximum retardation point) to 11, the  $\Delta K_{\text{eff}}$  increased gradually with increasing the

$\Delta K$ , which was in good agreement with a gradual increase in the crack-growth rate after the stage 5. Thus, it is noted that the changes in the  $\Delta K_{\text{eff}}$  were closely associated with those in the  $da/dN$  (Fig. 1).

Four distinct slopes from the curve of  $da/dN$  vs.  $\Delta K$  were found, as shown in Fig. 1: (case1) a slope (between stage 1 and 2a, and stage 8 and 11) from pre-overload constant-amplitude crack growth; (case2) a slope indicating an initial acceleration right after the tensile overloading; (case 3) a slope showing a sharp decrease between stage 2c and 5; (case 4) a slope between stage 5 and 7, which is larger than that in the case 1, but smaller than that in the case 3. Note that the slope change in crack-growth rate is depending on the change in the  $\Delta K_{\text{eff}}$ , which is a function of the COL. As shown in Fig. 6a, the COL in the constant-amplitude crack-growth without overload decreased slowly with increasing the  $\Delta K$  (see the COL change in the stage 1–2a and 8–11), and, thus, the change in the  $\Delta K_{\text{eff}}$  was also increased slowly. After a single tensile overload was introduced, very low COL was obtained, resulting in a sharp increase of  $\Delta K_{\text{eff}}$ . In the case 3, the COL increased so fast with a short increment of crack length (i.e., 0.6 mm from an overload point), which resulted in a sharp decrease of  $\Delta K_{\text{eff}}$ . Likewise, in the case 4, the gradual decrease of COL, which has higher reduction rate than that in the case 1, was examined. Thus, an increase rate in the  $\Delta K_{\text{eff}}$  from stages 5 to 8 is faster than that in the case 1. It can be noted that the change of  $\Delta K_{\text{eff}}$  shown in Fig. 6b was exactly corresponding to the slope change of experimentally measured crack-growth rate, as exhibited in Fig. 1.

To investigate the applicability of  $\Delta K_{\text{eff}}$  as the actual fatigue-crack-tip-driving force, the crack-growth rate ( $da/dN$ ) was plotted as a function of  $\Delta K_{\text{eff}}$ , as presented in Fig. 6c. The crack-growth rate had a good correlation with  $\Delta K_{\text{eff}}$  following a linear line, which suggests that  $\Delta K_{\text{eff}}$  is desirable for the actual fatigue-crack-tip-driving force.

### 3.4 *Residual-stress evolution near the crack tip through the retardation period*

Figure 7 shows the longitudinal residual stress distribution as a function of the distance from the overload point. Note that the overload point is corresponding to the crack-tip position at the stage 2. In Fig. 7a, the compressive residual stresses with a maximum of about  $-70$  MPa were measured near a fatigue crack tip ( $-4 \sim 1$  mm) at the stage 2a, right before overloading. After an application of a single tensile overload, a relatively much larger compressive residual stresses were observed in a larger range from the crack tip ( $-4 \sim 4$  mm). The highest compressive residual stress of  $-225$  MPa was examined at  $0.5$  mm ahead of the crack tip.

Figure 7b shows the residual stress evolution after the tensile overloading. As the fatigue crack propagates through the retardation period, the compressive residual stresses were relaxed and became smaller.

### 3.5 *Effects of compressive residual stress and crack-tip blunting on the crack-opening load*

After a tensile overload was applied, the COL was gradually changed from stages 2c to 8, as exhibited in Fig 6a. The change in the COL within this period is associated with the combined effect between large compressive residual stress and the crack-tip blunting. At the stage 5, the crack length was increased to  $0.6$  mm from the overload point (i.e., the crack-tip blunting region). From the neutron-diffraction measurement, it revealed that large compressive residual stress was applied in this closed crack. To make the crack tip fully open, the fatigue crack should overcome this large compressive residual stress field applied in the wake of the crack, and, thus, higher COL is required. Furthermore, the observed crack-arrest load,  $0.35 P_{\max}$ , at the stage 5 would be associated with a load value to remove this large compressive residual stress field.

The crack-tip blunting could be considered as another factor to influence the crack arrest and the determination of the COL. It is known that the crack-tip blunting behaves like a notch. As the load increases, the stress field would be initially concentrated on a blunting region, which would reduce the actual magnitude of the stress applied in the crack wake as well as the crack-tip position. When a higher load is applied, stress fields become large enough to open the closed crack face and the stress concentration is transferred with the gradual crack opening from the overload point to the crack-tip position. If the large compressive residual stress is also applied in the closed crack ahead of the crack-tip blunting, much higher load should be imposed to reach a certain stress value to open the closed crack face. Therefore, the crack arrest could be observed until a required stress value is obtained.

It should be pointed out that the transfer of stress concentration depends on both the crack length grown from the crack-tip blunting and the magnitude of compressive residual stress. If an actual crack-tip position is very close from an overload point (e.g., between the stage 2c and 3), the crack face will be open with a lower load. In contrast, if the crack-tip position is far away from an overload point (stage 8), the stress can easily concentrate on the crack tip with increasing the applied load. Thus, the closed crack face will be also open with a lower load. It might be thought that there is a certain critical crack length away from the overload point, similar to the critical crack length of the fatigue threshold region. The stage 5 is usually observed at 0.3–0.6 mm from the overload point. This distance might be thought as the critical point where the combined effects between large compressive residual stress and crack-tip blunting are maximized. In summary, the combined effects between large compressive residual stress and crack-tip blunting are responsible for the observed change in the COL within the retardation period, resulting in the stress transfer from an overload point to the crack-tip position.

## 5. Conclusions

Electric-potential and neutron-diffraction experiments were carried out to investigate the overload-induced fatigue-crack-growth mechanisms. The main results are as follows:

1. Immediately after the tensile overload was applied, the crack tip became blunt and the large compressive residual stresses were observed around the crack tip.
2. An initial acceleration of the crack-growth rate is due to the crack-tip blunting.
3. In the maximum retardation point (stage 5), the highest crack-opening load was examined, indicating the smallest  $\Delta K_{\text{eff}}$  value.
4. The combined effects between large compressive residual stress and crack-tip blunting are responsible for the change of the crack-opening load within the retardation period, resulting in the stress transfer from an overload point to the crack-tip position.
5. The crack-growth rate can be normalized with  $\Delta K_{\text{eff}}$ . Therefore  $\Delta K_{\text{eff}}$  is desirable as a fatigue-crack-tip-driving force.
6. The results show that the combined effects between compressive residual stress and crack-tip blunting are the main cause for the overload-induced transient crack-growth behavior based on the crack-closure approach.

## **Acknowledgements**

This work is supported by the US National Science Foundation (NSF) International Materials Institutes (IMI) Program under contract DMR-0231320, with Drs. U. Venkateswaran, D. Finotello, and C. Huber as the program directors. Author would like to thank Dr. Rogge of Chalk River Laboratories, Canada for his kind help during neutron experiments.

## References

- [1] W. Elber, *Eng. Fract. Mech.* 2 (1970) 37-45
- [2] W. Elber, *ASTM STP 486*, pp. 230-242
- [3] C. Bathias and M. Vancon, *Eng. Fract. Mech.* 10 (1978) 409-424
- [4] R.E. Jones, *Eng. Fract. Mech.* 5 (1973) 585-604
- [5] J.F. Knott and A.C. Pickard, *Met. Sci* (Aug/Sept, 1977) 399-404
- [6] J. Schijve and D. Broek, *Aircr. Eng.* 34 (1962) 314-316
- [7] C.M. Hudson, and H.F. Hardrath, *NASA Tech. Note D-960* (1961)
- [8] A. Steuwer, L. Edwards, S. Pratihari, S. Ganguly, M. Peel, M.E. Fitzpatrick, T.J. Marrow, P.J. Withers, I. Sinclair, K.D. Singh, N. Gao, T. Buslaps, J.-Y. Buffiere, *Nucl. Instr. and Meth. in Phys. Res. B* 246 (2006) 217-225.
- [9] M.C. Croft, N.M. Jisrawi, Z. Zhong, R.L. Holtz, K. Sadananda, J.R. Skaritka, T. Tsakalakos, *Int. J. Fatigue* 29 (2007) 1726-1736.
- [10] S.Y. Lee, R.I. Barabash, J.-S. Chung, P.K. Liaw, H. Choo, Y. Sun, C. Fan, L. Li, D.W. Brown, G.E. Ice, *Metall. Mater. Trans. A* 39 (2008) 3164-3169.
- [11] S.Y. Lee, H. Choo, P.K. Liaw, E.C. Oliver, A.M. Paradowska. *Scripta Mater.* 60 (2009) 866-869.
- [12] *ASTM Standard E647-99: Standard Test Method for Measurement of Fatigue Crack-Growth Rates*, 2000 Annual Book of ASTM Standards, Vol. 03.01, 591-630
- [13] P.K. Liaw, T.R. Leax, R.S. Williams and M.G. Peck, *Metall. Trans.* 13 (1982) 1607-1618
- [14] H. H. Johnson: *Materials Research and Standards*, 5 (1965) 442-445.
- [15] R. O. Ritchie and K. J. Bathel: *Inter. Journal of Fracture*, 15 (1979) 47-55.
- [16] C.K. Clarke and G.C. Cassatt, *Engng. Frac. Mech.* 9 (1977) 675-688

**Table caption**

Table 1 Details on eleven crack-growth stages marked in Fig. 1 (F: fatigue, OL: overload, EP: electric potential, ND-RS: neutron-diffraction residual stress). Each experiment were carried out at the marked stage with “O”

## Figure captions

- Figure 1 The change in the crack-growth rates ( $da/dN$ ) as a function of the stress-intensity-factor range ( $\Delta K$ ).
- Figure 2 Schematic of (a) a Haystelloy C-2000 compact-tension specimen, (b) spatially-resolved neutron-diffraction measurement positions along the direction of the crack propagation ( $x$ ).
- Figure 3 Electric-potential change during a single loading-unloading cycle (a) at the stage 2a, a cycle right before the tensile overloading, (b) at the stages 2b (a cycle during overloading) and 5 (a maximum retardation point)
- Figure 4 SEM micrographs (a) before, (b) after the overloading, and (c) at the stage 5.
- Figure 5 Electric-potential change during a single loading-unloading cycle at various crack-growth stages marked in Fig. 1.
- Figure 6 (a) Crack-opening load variations, (b)  $\Delta K_{\text{eff}}$  vs.  $\Delta K$ , and (c)  $da/dN$  vs.  $\Delta K_{\text{eff}}$  at various crack-growth stages marked in Fig. 1.
- Figure 7 Longitudinal residual-stress profiles at (a) the stages 2a and 2c; (b) the stages 2c, 5, and 7 measured along the crack-growth direction ( $x$ ).

Table 1

Growth stages	Crack length (mm)	$\Delta K$ (MPa.m <sup>1/2</sup> )	Description	Various measurements	
				EP	ND – RS
1	18	32.41	F	○	
2	20	35.90	2a (right before OL): F	○	○
			2b (during OL): F+OL	○	
			2c (right after OL): F+OL+F	○	○
3	20.19	36.26	F+OL+F	○	
4	20.33	36.52		○	
5	20.6	37.04		○	○
6	21.4	38.64		○	○
7	22.3	40.56		○	○
8	24.2	45.12		○	
9	26.5	51.86		○	
10	27.6	55.70		○	
11	30	66.02		○	

Figure 1

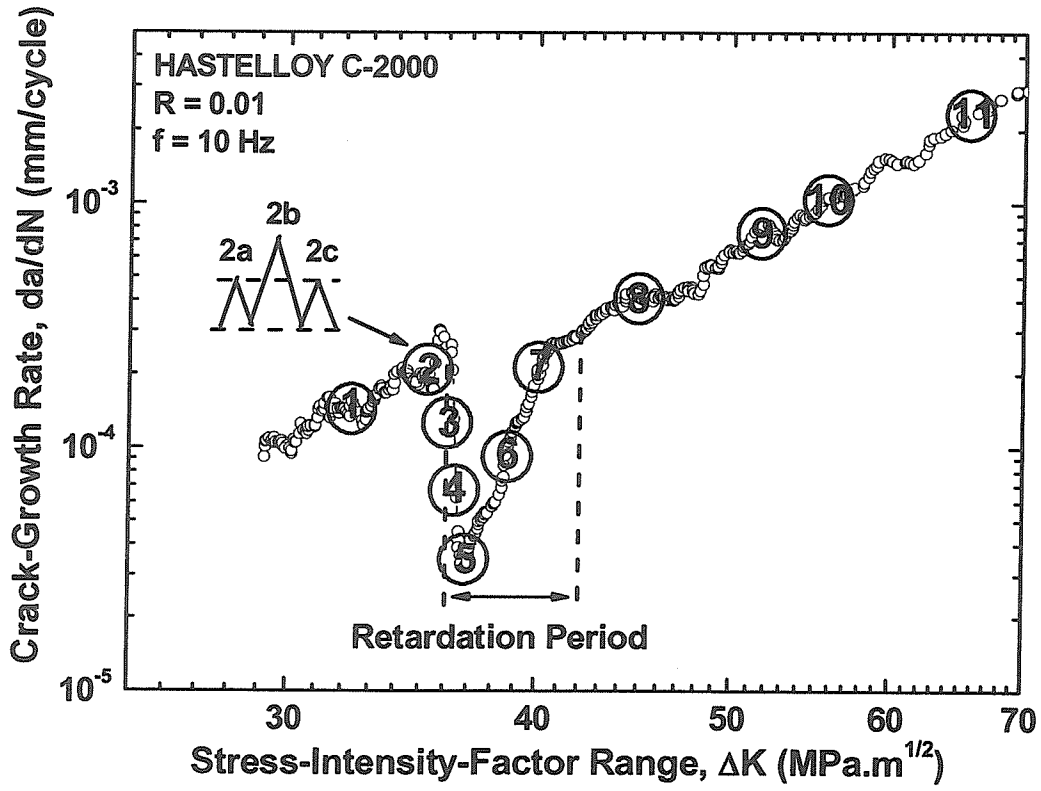
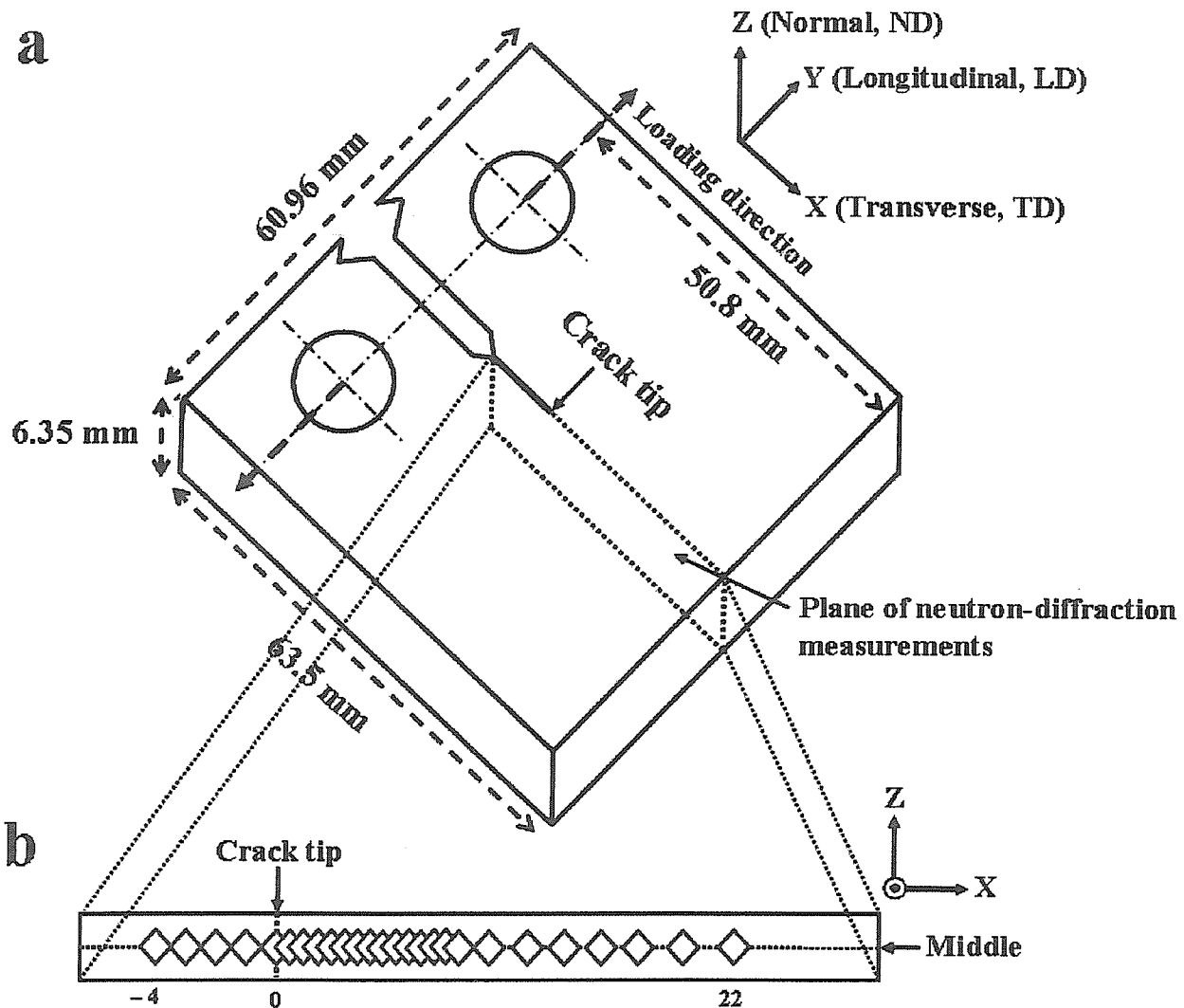


Figure 2



Spatially-resolved neutron-diffraction measurement positions:

-4, -3, -2, -1, 0 (Tip), 0.5, 1, 1.5, 2, 2.5, 3, 3.5, 4, 4.5, 5, 5.5, 6, 6.5, 7, 8, 10, 12, 14, 16, 19, 22 mm

Figure 3

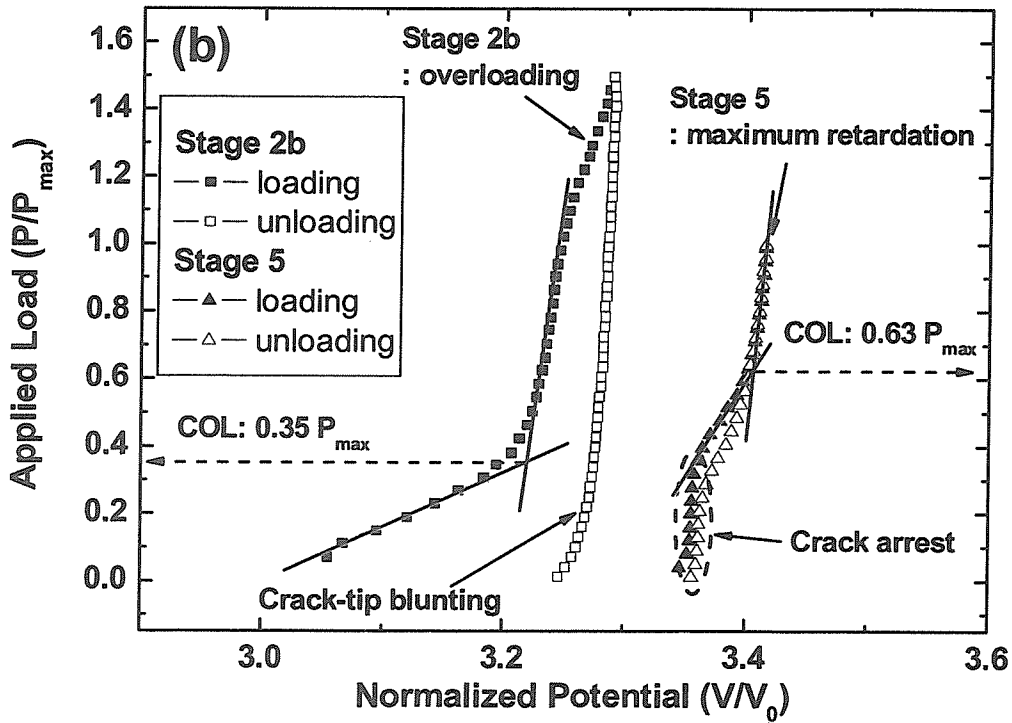
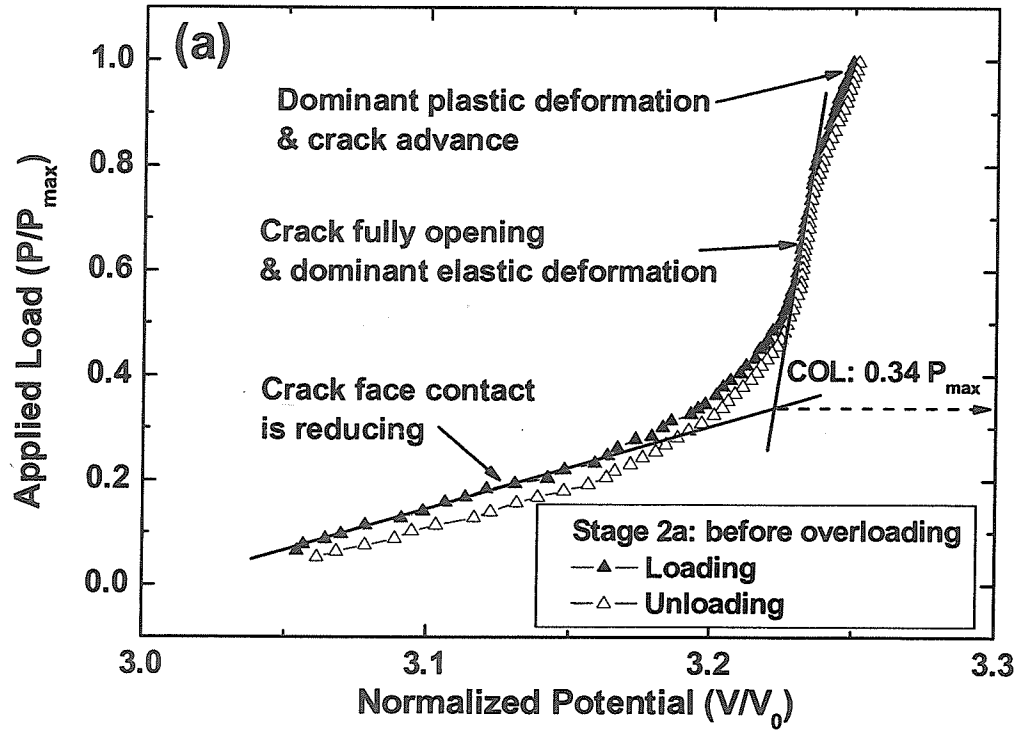
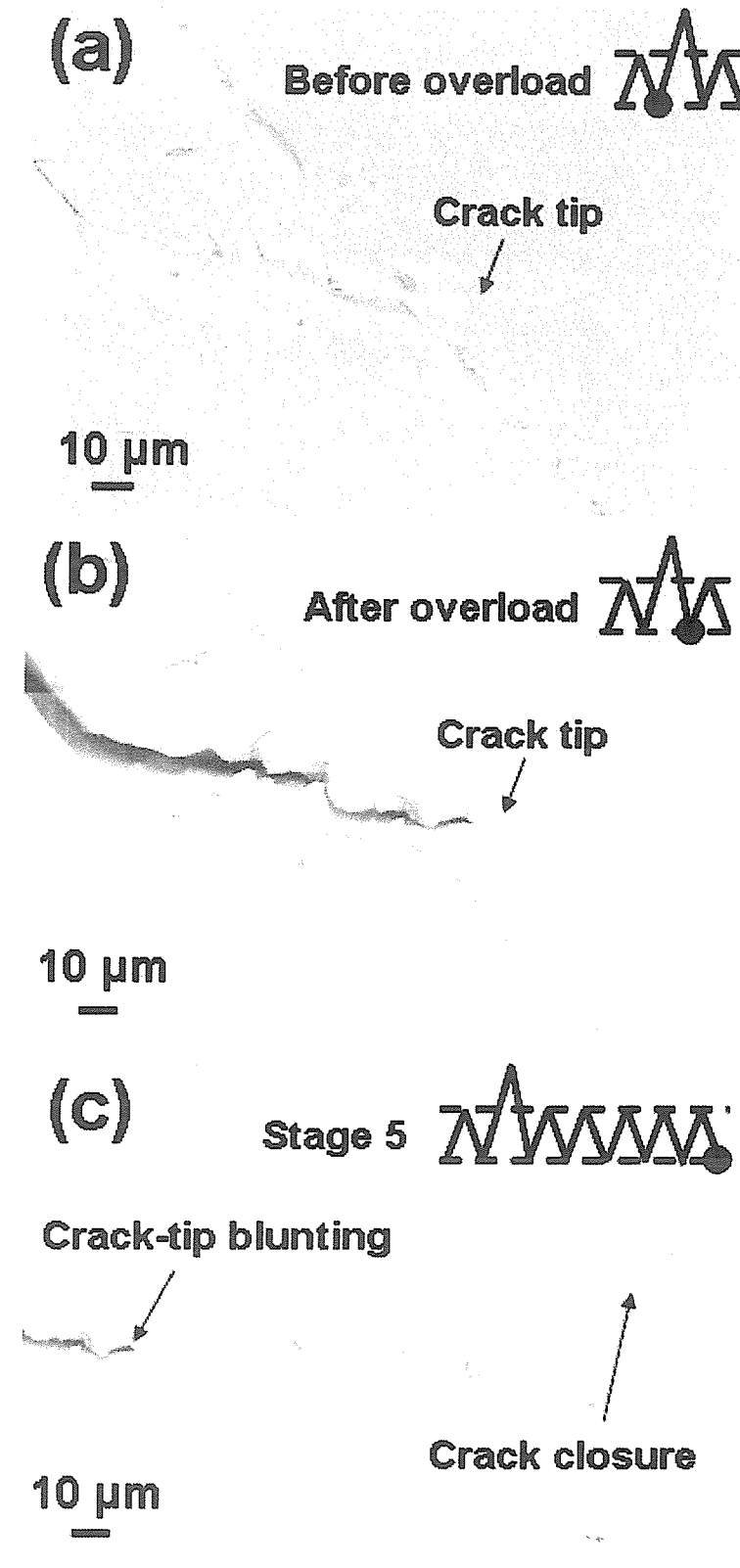
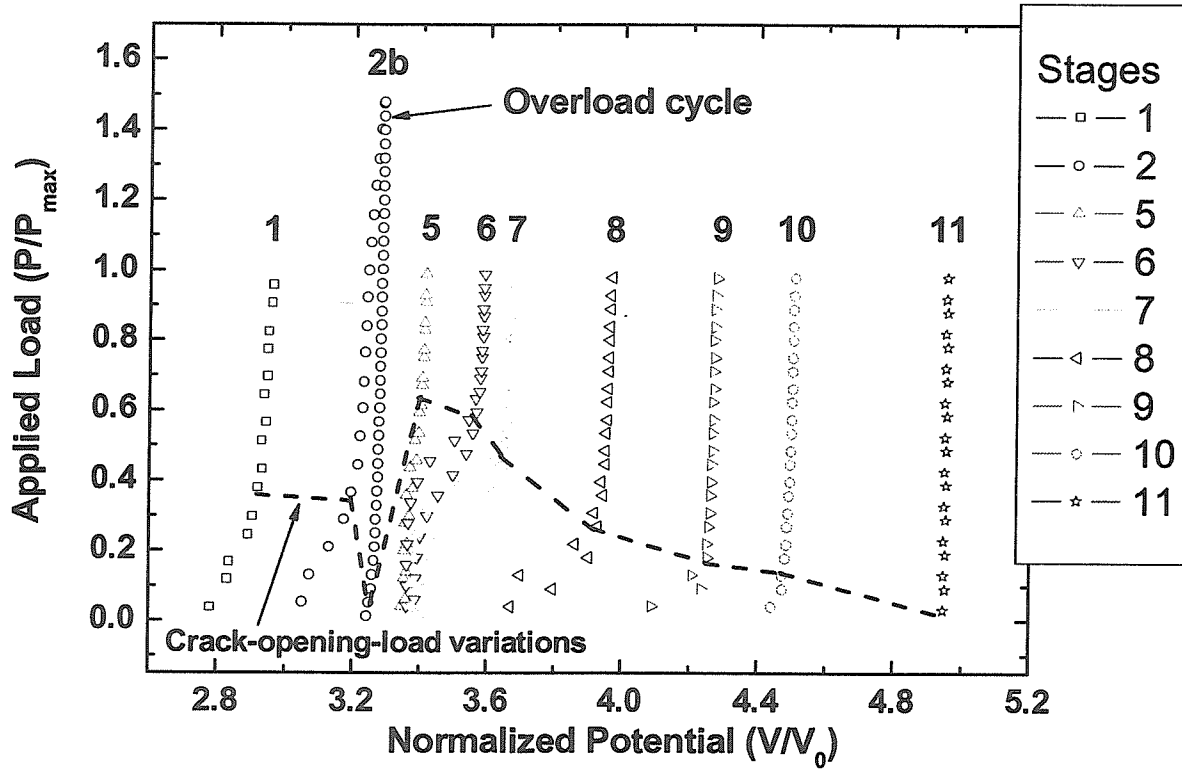


Figure 4



**Figure 5**



**Figure 6**

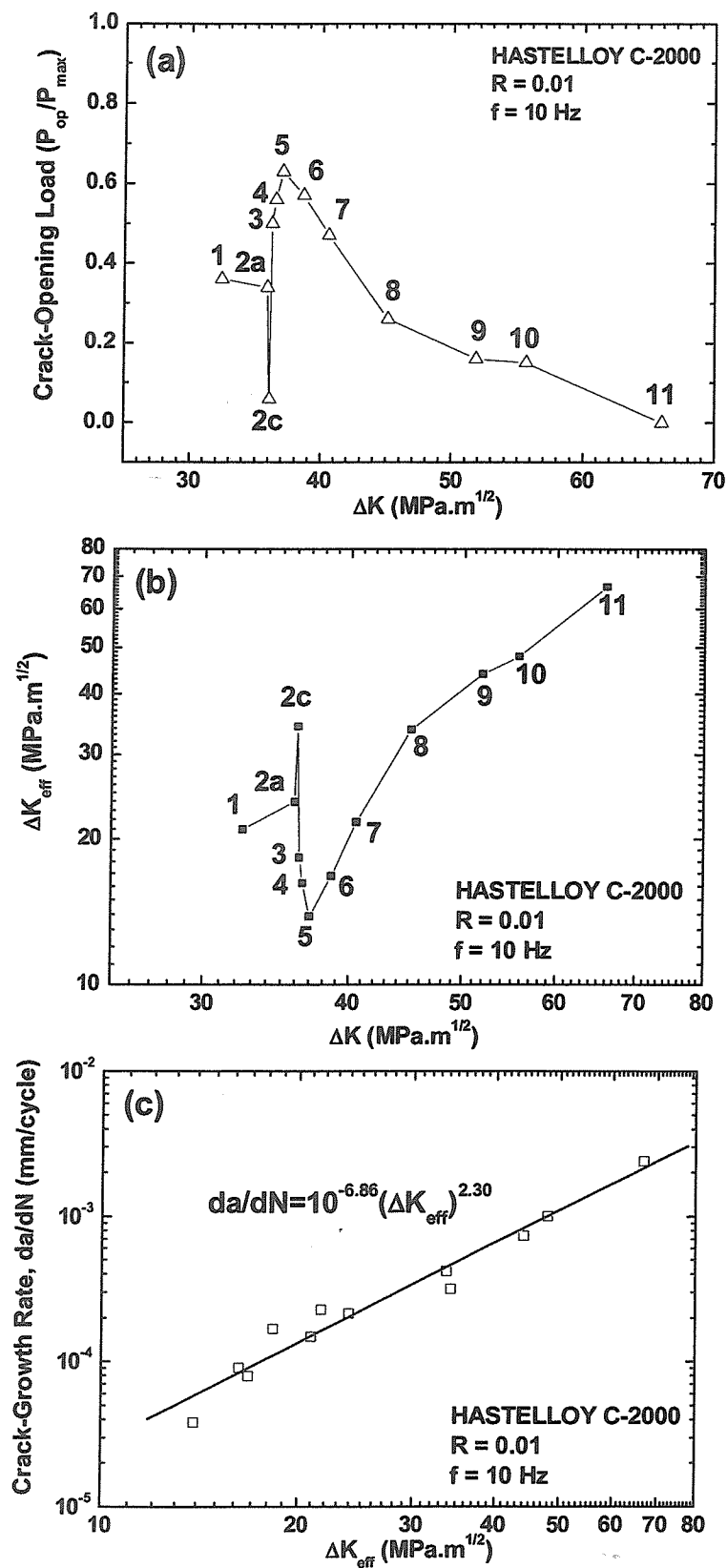


Figure 7

